



**Understanding the effects of fabrication process on
BaZr_{0.9}Y_{0.1}O_{3-δ} grain-boundary chemistry using atom
probe tomography**

Journal:	<i>Journal of Materials Chemistry C</i>
Manuscript ID	TC-ART-09-2022-004093.R1
Article Type:	Paper
Date Submitted by the Author:	09-Mar-2023
Complete List of Authors:	Clark, Daniel; Colorado School of Mines, Metallurgical and Materials Engineering; CoorsTek Inc Diercks, D.; Colorado School of Mines, Metallurgical and Materials Engineering Ricote, Sandrine; Colorado School Of Mines, Mechanical Engineering Tauer, Tania; The foundry 10 Sullivan, Neal; Colorado School Of Mines, Mechanical Engineering; Colorado School of Mines Medlin, Will; University of Colorado, Chemical and Biological Engineering Gorman, Brian; Colorado School of Mines, Metallurgical and Materials Engineering O'Hayre, Ryan; Colorado School of Mines, Dept of Metallurgical and Materials Engineering

Understanding the effects of fabrication process on BaZr_{0.9}Y_{0.1}O_{3-δ} grain-boundary chemistry using atom probe tomography

Received 00th January 20xx,
Accepted 00th January 20xx

Daniel R. Clark^{a,b*}, David R. Diercks^a, Sandrine Ricote^c, T. Tauer Dearden^d, Neal P. Sullivan^c, J. Will Medlin^e, Brian P. Gorman^a, and Ryan P. O'Hayre^{a*}

DOI: 10.1039/x0xx00000x

Proton-conducting oxides, such as BaZr_{0.9}Y_{0.1}O_{3-δ} (BZY10), are receiving significant scientific attention for application in a variety of electrochemical applications. It has been shown that the synthesis route has a significant effect on the ionic behavior of these materials, especially the grain boundaries (GB). In this study, laser-pulsed atom probe tomography (APT) is used to characterize the GB chemistry of BZY10 samples prepared by four different methods: (1) spark plasma sintering (SPS), (2) conventional sintering followed by high-temperature annealing (HT), (3) conventional sintering with NiO used as a sintering aid (SSR-Ni), and (4) solid-state reactive sintering of oxide precursor powders with NiO as a reactive sintering aid (SSRS-Ni). Oxygen depletion (corresponding to oxygen vacancy accumulation) was observed at every GB in this study, consistent with the positive space-charge GB region commonly assigned to these materials. In contrast to the consistent trends associated with oxygen depletion, cation constituents showed varying segregation/depletion behaviors. The samples that used NiO revealed Ni preferentially segregating to the GB. The most common impurities in BZY10 are Al, Fe, Mg, Si, and Sr, all of which generally accumulate at GBs. In order to quantify these chemical trends, the APT method was optimized for this material supplemented with understanding from density functional theory (DFT). This APT study reveals the complexity of BZY10 GB chemistry and shows that even adjacent GBs in the same material can sometimes show surprisingly different GB chemistry.

1. Introduction

Proton-conducting ceramics such as yttrium-doped barium zirconate (BZY) and yttrium-doped barium cerate (BCY) have strong potential for applications such as intermediate-temperature fuel cells, steam electrolysis, methane dehydroaromatization (MDA), and hydrogen production.^{1–12} BZY is receiving particular attention due to its improved stability compared to BCY in H₂O- and CO₂-containing environments,^{2,13–16}. However, this stability comes at the cost of sintering challenges and higher grain-boundary (GB) resistance.¹⁷ These issues have motivated the development of a variety of fabrication methods in an attempt to produce dense, large-grained BZY materials with lower grain boundary resistance. As shown by Ricote et al.,¹⁸ these different processing methods can lead to dramatic variations in the GB and bulk conductivity of

BaZr_{0.9}Y_{0.1}O_{3-δ} (BZY10). In Ricote's work, the results from four different BZY10 fabrication techniques were compared:

- spark plasma sintering at 1700 °C (SPS);¹⁹
- solid-state reaction at 1200 and 1400 °C followed by a sintering at 1720 °C to produce phase-pure BZY10 powder, followed by high-temperature annealing at 2200 °C (HT) to produce dense samples;²⁰
- solid-state reaction at 1585 °C to produce phase-pure BZY10 powder, followed by sintering at 1600 °C with 1 wt. % NiO added as a sintering aid to produce dense pellets (SSR-Ni);¹⁸
- single-step solid-state reactive sintering at 1535 °C directly from BaCO₃, ZrO₂, and Y₂O₃ precursor powders with 1 wt. % NiO as a reactive sintering aid (SSRS-Ni).^{18,21}

Electrochemical impedance spectroscopy (EIS) studies revealed >10X differences in the bulk and the GB conductivities between samples produced by these four methods. Some of the absolute conductivity variations between sample types could be explained by differences in microstructure (e.g. grain size). However, substantial variations were also observed in the specific (i.e. area-normalized) bulk-to-GB ratios between sample types. This observation suggests that the different fabrication processes likely lead to substantial differences in the GB chemistry, with a consequent effect on the specific GB resistance.

In order to examine this hypothesis in further detail, the present work applies laser-pulsed atom probe tomography

^a Colorado Center for Advanced Ceramics, Colorado School of Mines, 1500 Illinois St., Golden, CO 80401, USA

^b Department of Chemistry, Centre for Materials Science and Nanotechnology, University of Oslo, Oslo, Norway

^c Department of Mechanical Engineering, Colorado School of Mines, 1500 Illinois St., Golden, CO 80401, USA

^d Foundry10, 4545 Roosevelt Way, Suite #500; Seattle, WA 98105, USA

^e Department of Chemical and Biological Engineering, University of Colorado Boulder, Boulder, CO 80303, USA

† Footnotes relating to the title and/or authors should appear here.

Electronic Supplementary Information (ESI) available: [details of any supplementary information available should be included here]. See DOI: 10.1039/x0xx00000x

(APT^{22–24}) to probe the grain boundary chemistry of the same four BZY10 samples previously interrogated in the Ricote study. The goal of the present work is thus to uncover potential linkages between the BZY10 fabrication method, GB chemistry, and the resulting ionic conduction properties.

Using focused-ion beam (FIB) based tip fabrication methods, APT specimens can be produced that contain a GB within the needle-shaped volume. See supplemental information for further details. We have previously demonstrated that this approach can be used to extract nm-scale spatial information and very high chemical resolution from the GB regions of BZY-based proton-conducting ceramics.²⁵ In contrast, traditional characterization techniques, such as scanning transmission electron microscopy with energy dispersive x-ray spectroscopy (STEM-EDS), generally lack the chemical sensitivity to analyze GB chemistry quantitatively. This is due in large part to the challenges of directly correlating the number of measured x-ray counts with a specific composition and the two dimensional projection through a three dimensional structure.

However, for APT, it is essential that the experimental conditions are optimized for the analyzed material. Because BZY is a multi-cation material, this presents challenges in obtaining accurate chemical quantification due to the differing fields required for removing each cation/anion species. Therefore in this study, the effect of the applied field on the stoichiometric ratios of two common compositions of proton-conducting ceramics, BaZr_{0.9}Y_{0.1}O_{3-δ} (BZY10) and BaCe_{0.2}Zr_{0.7}Y_{0.1}O_{3-δ} (BCZY27) was examined in order to gain confidence that APT can be used for these materials. In APT, there is a relationship between laser pulse energy and standing bias for a given detection rate; as the laser energy decreases, the required standing bias increases and changes in anion stoichiometry have been observed^{26,27}. Since the only difference between the two materials studied here (BZY10 vs BCZY27) is the substitution of cerium for some of the zirconium, this study also reveals the effects of the differing Ce-O and Zr-O bond strengths on the optimal laser energy/applied field. Density functional theory (DFT) is used to help understand the differing results between BZY10 vs. BCZY27, providing insight into the tradeoffs needed to achieve accurate measurement of the correct stoichiometry for a given material. This allows for a much more meaningful analysis of the differing GBs in the BZY material.

2. Experimental

2.1 Materials Synthesis

As described above, in this work, we used APT to examine the grain boundary chemistry of BZY10 samples prepared by four different synthesis methods (SPS, HT, SSR-Ni, and SSRS-Ni). Because interpretation of the APT results requires an understanding of the nuances in the four synthesis methods, they are briefly detailed below. For further details, readers are referred to the original papers.^{18–20}

SPS:^{18,19} SPS samples were prepared from BaCO₃ (Aldrich, 99+%), Y₂O₃ (Sigma-Aldrich, 99.99%), and YSZ (Sigma-Aldrich,

submicron powder; 99.5%, 5.3 mol. % of yttria) powders mixed in stoichiometric amounts and ball milled for 20 h with ZrO₂ milling media. After calcination in air at 1400 °C for 24 h in an alumina crucible, SPS was carried out using a Sumitomo SPS 2080 provided by Plateforme PNF2, Université Paul Sabatier, CIRIMAT, Toulouse, France. The BZY10 powder, without binding material, was set in a graphite die and sintered under vacuum (roughly 1 Pa). The experiments were done at 1700 °C for 5 min using a uniaxial pressure of 100 MPa. The heating rate for all SPS experiments was maintained at around 150 °C•min⁻¹ with a natural cooling rate of 100 °C•min⁻¹. The temperature was controlled by an optical pyrometer focused on a small hole (1.8 mm diameter, 3 mm depth) at the surface of the die.

HT:²⁰ The HT sample was prepared from BaCO₃ (Fluka 99%), Y₂O₃ (Stanford Materials, 99.9%), ZrO₂ (Tosoh, 99.9%) powders mixed in stoichiometric amounts, and ball milled with 3 mm-ZrO₂ milling media. The powder was calcined in air at 1200 °C for 10 h then dry ball-milled for another 48 h before an additional calcination at 1400 °C for 10 h. The fully calcined powder was milled in a planetary mill (200 rpm) in a ZrO₂ container for 3 h then isostatically pressed into a rod and sintered at 1720 °C for 24 h in a bed of pre-sintered BZY10 powder. The as-sintered rod was annealed in an optical floating zone furnace (FZ-T-10000-H-IV-VP-PC, Crystal System Corp., Japan) using four 1000 W halogen lamps as a heat source. The focused light was moved along the rod (back-and-forth) with a rate of 5 mm/h, achieving a maximum temperature in the hot zone of approx. 2200 °C. The annealing was performed in oxidizing atmosphere (5% O₂ in Ar) at a pressure of 2 bars and a gas flow rate of 250 ml/min.

SSR-Ni¹⁸: The SSR-Ni sample was prepared using stoichiometric proportions of BaSO₄ (Solvay), ZrO₂ (AMR China) and Y₂O₃ (HJD Int., Ultrafine 99.99+%) which were blended in acetone for 24 h. After drying, the powder mixture was calcined at 1585 °C for 6 h in an alumina crucible, and then ball milled using ZrO₂ milling media and sieved through a 120 mesh screen. NiO at 1 wt. % was added to the calcined BZY10 powder as a sintering aid. A binder and dispersant solution of PeOx (poly(2-ethyl-2-oxazoline)), MW 5000 binder and Kellogg (fish oil) was added and the mixture was blended for an additional hour. The dried powder was sieved through an 80 mesh screen, and pellets were uniaxially pressed (60 MPa) and sintered in air at 1600 °C for 24 h on a Ni-YSZ substrate without a packed bed of powder.

SSRS-Ni¹⁸: The SSRS-Ni sample was prepared via solid-state reactive sintering (SSRS)²¹ by mixing BaCO₃ (Alfa Aesar, 99.95% metal basis), ZrO₂ (AMR China), and Y₂O₃ (HJD Int., Ultrafine 99.99+%) in stoichiometric amounts, with the addition of 1 wt. % NiO (Novamet, Inco F-Grade). After ball milling with ZrO₂ milling media for 24 h, the powder was mixed with 1 wt. %

solution of PeOx, MW 5000 binder, and Kellogg and sieved through a 20 and 80 mesh screen. The pellets were uniaxially pressed (60 MPa) into a 20 mm disk and sintered at 1535 °C for 8 h. Each sample was used for conductivity experiments (long duration at intermediate temperatures in moist 5% H₂ balanced Ar and very slowly cooled down to room temperature—see Ref. 14 for details) before APT analysis.

2.2 APT Analysis

For each sample, APT specimens specifically targeted to contain a GB region were created using a focused ion beam (FIB) lift-out technique (see Supplementary Information for more detail). Briefly, the sharp tip-like APT specimens were prepared from the bulk BZY10 samples using an FEI Helios NanoLab™ 600i focused ion beam (FIB) microscope using a standard wedge lift-out technique and annular milling patterns from the centers of each pellet (to avoid surface contamination/changes). Initially, tips were sharpened using a 30 kV Ga-ion beam and then subsequently cleaned with a 2.0 kV Ga-ion beam to minimize Ga damage to the surface. Multiple APT specimens were prepared from each sample, meaning that the multiple grain boundaries analyzed for each sample originated from within close proximity (<15 μm) to each other. Fig. S1 illustrates a FIB sample of BZY10 SSR-Ni, outlining the approximate locations of each APT specimen produced from this lift-out.

APT was performed in a Cameca LEAP 4000X Si system equipped with a 355 nm wavelength laser with a spot size less than 1 μm at full-width half-maximum (FWHM). An optimized laser energy of 10 pJ was used with a pulse frequency of 625 kHz and a specimen base temperature of 40 K. In order to quantitatively compare grain boundary vs. bulk composition, a region of interest (ROI) was designated that contained the GB region for each APT dataset. Average mass spectra were then analyzed inside and outside the ROI. Quantification of the APT data depended, in part, on the deconvolution of overlapping peaks in the mass spectra. Peak deconvolution involved fitting of the subsidiary isotopic mass peaks for overlapping elements in concert with the known natural isotopic abundances of these elements. For further details on the APT experimental methods, peak deconvolution, and ROI selection please see the Supplementary Information.

2.3 Stoichiometric analysis via correlative techniques

Stoichiometries of the BZY10 and BCZY27 samples (material synthesis found in Supplementary Materials) were measured using XRF, calibrated against several known standards (Phillips MagiX). The exterior surfaces of the samples, as well as standard BZY10 and BCZY27 samples, were also analyzed directly by Laser Ablation ICP-OES (Spectro Acros FHS13 with a Cetac LSX-500 Laser Ablation System). The spectral peaks at the wavelengths corresponding to Ba, Zr, Ce, and Y were measured. The results were then compared to standard samples to obtain absolute levels of metal oxides in units of weight percent.

3. Results and discussion

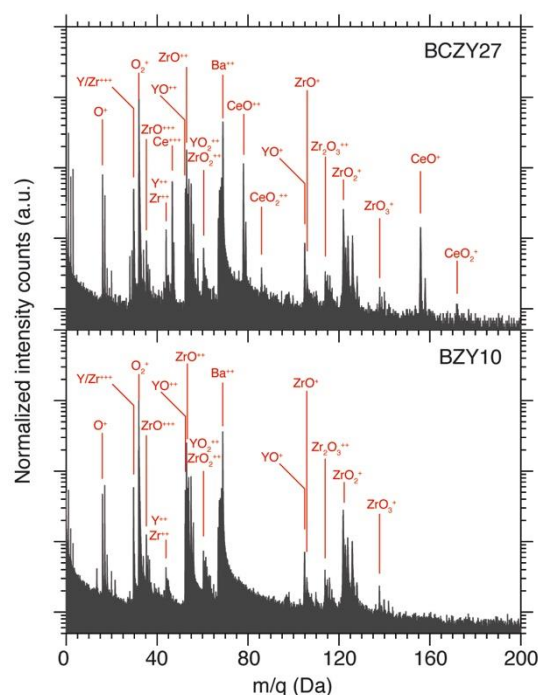


Fig. 1. Labeled APT mass spectra of BZY10 and BCZY27 collected at 10 pJ. The mass spectra are normalized to the intensity of the O₂⁺ (32 Da) peak with no background correction. Some minor peaks, including impurities, are not labeled for clarity.

3.1 Accurately quantifying stoichiometry

Representative APT-measured mass spectra of the bulk BZY10 and BCZY27, both obtained at a laser energy of 10 pJ, are shown in Fig. 1. The most abundant ions and ion clusters have been labeled. Small impurities of nickel (intentionally added as a sintering aid for BCZY27), silicon, aluminum, strontium, and hafnium were found in the specimens at levels below 1 at. % and are common impurities found in the precursor powders. These are not labeled in the mass spectra for clarity. Individual mass spectra and a discussion on the behavior of ions as a function of laser energy can be found in the Supplementary Materials (Fig. S2 and S3).

Fig. 2 plots the deviations between the “apparent” (measured from APT) and “actual” (measured from standards-calibrated XRF and ICP-OES) stoichiometries for Ba, Ce, Zr, Y, and O in the BZY10 and BCZY27 samples. The detected Si, Al, Ni, Sr and Hf are not included in this analysis. Grey regions denote a conservative estimate of the error associated with our standards-calibrated XRF determination of stoichiometry (~±2 at. %). Thus, APT stoichiometry measurements falling within the grey band are deemed to be approximately as accurate as those from the calibrated XRF measurement. The scatter in the APT data is attributed to variations in specimen tip shapes, which leads to variations in the electric fields for a given laser energy. Even though the same sharpening routine was used with all of the tips, the final tip shape varies based on factors such as fluctuations in the FIB ion beam current density/probe size and crystal-orientation-dependent milling speed.

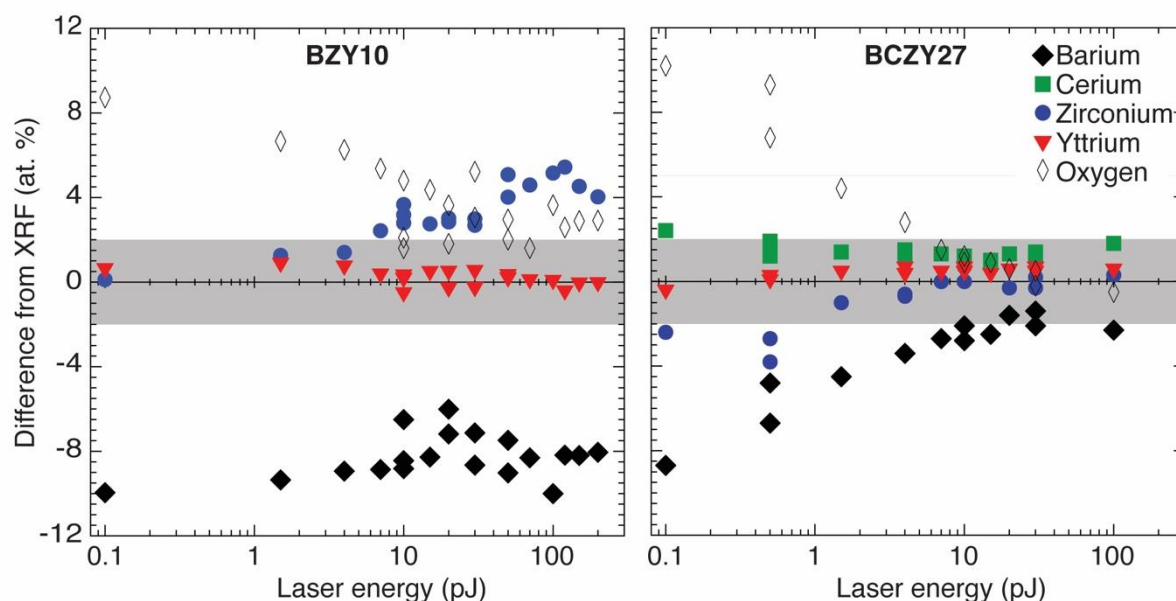


Fig. 2. Deviation between the “apparent” (measured from APT) and “actual” (measured from standards-calibrated XRF and ICP-OES) stoichiometry for Ba, Ce, Zr, Y, and O in the BZY10 and BCZY27 samples as a function of the laser energy.

Bond		Ba-O	Zr-O	Ce-O	Y-O
Energy (eV)	BaZrO ₃	-0.73	-3.11	-	-2.45
	BaCeO ₃	-0.71	-	-2.54	-2.76

Table 1. Bond energies (eV) calculated by DFT (VASP) for 12.5% yttrium-doped barium zirconate (BaZrO₃) and 12.5% yttrium-doped barium cerate (BaCeO₃).

In order to help understand the results of Fig. 2, Table 1 presents the oxygen bond energies in both yttrium-doped BaCeO₃ and BaZrO₃ calculated by DFT (methods detailed in Supplementary Materials). As can be seen in Fig. 2, the oxygen stoichiometry measured by APT for both BZY10 and BCZY27 is higher than expected at low laser energies, while the Ba stoichiometry is lower than expected. This is attributed to the relative weakness of the Ba-O bond compared to the Zr-O and Y-O bonds (Table 1). Under the higher DC standing bias required at low laser energies, we hypothesize that a significant amount of weakly-bound Ba evaporates between pulses and thus is not used in analysis, resulting in an apparent Ba-cation loss and a corresponding apparent anion (oxygen) enrichment. The Ba evaporation hypothesis is corroborated by the prominent tail on the Ba⁺ peak mass spectrum (larger than all the other species) shown in Fig. S2 and Fig. S3, which is a hallmark of post-pulse evaporation caused by poor thermal dissipation in thermal insulators. At higher laser energies, the APT-measured oxygen-ion stoichiometry decreases and approaches that of the XRF standard, although an apparent slight enrichment is maintained. While a decrease in anion concentration with increasing laser energy is consistent with literature^{26,28,29}, few studies have observed an apparent absolute enrichment in the APT-measured anion stoichiometry (most other studies have measured an apparent anion depletion)³⁰. We hypothesize that the apparent APT-measured anion enrichment is again connected to Ba volatility, and the fact that inter-pulse Ba

evaporation likely greatly exceeds the laser-induced oxygen atom sublimation that causes anion sub-stoichiometry. At higher laser energies, the background signals due to inter-pulse Ba evaporation decrease, as shown in Fig. S4.

One of the major observations from the above results is that for multiple cation (or anion) ceramics it may not be possible to achieve the correct quantification of all species simultaneously, which has previously been observed in InGaN and InAlN³¹. Due to the tradeoffs associated with the differing evaporation and detection rates between cation and anion species, for BZY10 it is not possible to identify a unique laser energy condition that yields the correct total stoichiometry for *all* species simultaneously. However, it is possible to identify laser energy ranges where good accuracy was obtained for one or more species at the same time. This means that the analysis conditions can be tailored toward the quantification of a particular species of interest. An additional concern is laser-induced redistribution of particularly mobile species during measurement. To investigate this potential issue, the standard deviations of the measured elemental compositions were calculated from twelve 8x8x8 nm sub-volumes randomly selected throughout each reconstruction for each of the laser energies. There was no clear trend in these values as a function of laser energy, although at lower laser energies (such as the 10 pJ used for the subsequent analyses of the various samples in this work) there was minimal spatial variation in the measured composition, indicating that there is no appreciable laser-induced segregation of mobile elements during measurement.

Interestingly, while there are many similarities in behavior between BZY10 and BCZY27, there are also a few important differences. In particular, BZY10 shows an optimal range of laser energies for oxygen quantification between ~7-100 pJ, while for BCZY27, this optimal range is between ~10-70 pJ. For BZY10, Zr quantification was optimal between 0.1 and 4 pJ, and deviates from stoichiometry with further increasing laser energy.

Because of this, ~ 10 - 20 pJ is deemed the most ideal laser energy range for BZY10 to maintain optimal oxygen stoichiometry while minimizing the Zr and Ba stoichiometric deviations. For the remainder of the APT results in this study, 10 pJ was used as the laser energy.

3.2 APT of the SPS sample

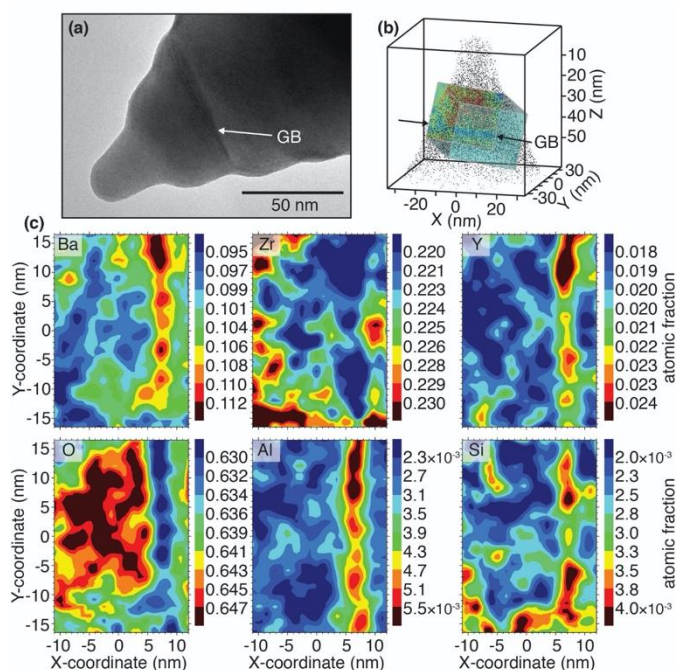


Fig. 3. APT analysis of SPS2. (a) Transmission electron microscopy (TEM) micrograph pre-APT analysis. (b) Region of interest (ROI) used for (c) elemental atomic fraction 2-D contour maps of Ba, Zr, Y, O, Al, and Si.

Two different grain boundaries from the SPS sample were examined by APT (SPS1 and SPS2). Fig. S6 (SPS1) and Fig. 3 (SPS2) provide the Ba, Zr, Y, and O elemental contour maps for these two specimens, as well as maps for Al and Si, which were the main impurities found in these specimens.

Oxygen depletion coupled with Ba, Y, and Al accumulation was observed at the GB of both SPS specimens. One of the samples (SPS2; Fig. 3c) showed a very slight Si accumulation at the GB. The Al impurity concentration ranged from ~ 2000 parts-per-million (ppm) in the bulk to ~ 6000 ppm at the GB, while the Si impurity concentration ranged from about 300 ppm in the bulk to as much as 4000 ppm at the GB. The powders for the SPS samples were calcined in alumina crucibles at 1400 °C; we hypothesize that this was the likely source of the Al impurities found in these specimens. There are several possible sources for the Si impurity, including contamination from the quartz-based mortar and pestle materials, trace impurities in the precursors as well as potential contamination from the MoSi_2 furnace elements used in the calcination step.

3.3 APT of the HT sample

Three different GBs from the HT sample were examined by APT (HT1, HT2, and HT3); these showed the most varied GB chemistry of all samples. The first two HT GB specimens, HT1 and HT2 (Fig. 4 and Fig. S7), showed similar behavior (Zr and O

depletion at the GB coupled to Ba and Y accumulation), but the third GB specimen, HT3 (Fig. 5) showed markedly different behavior: Ba, Y, and O depletion coupled to Zr accumulation. It is interesting to note that specimen HT3 originated from a GB only a few microns away from specimens HT1 and HT2. Thus, the three major cationic species showed opposite segregation behavior in the HT3 specimen compared to HT1 and HT2.

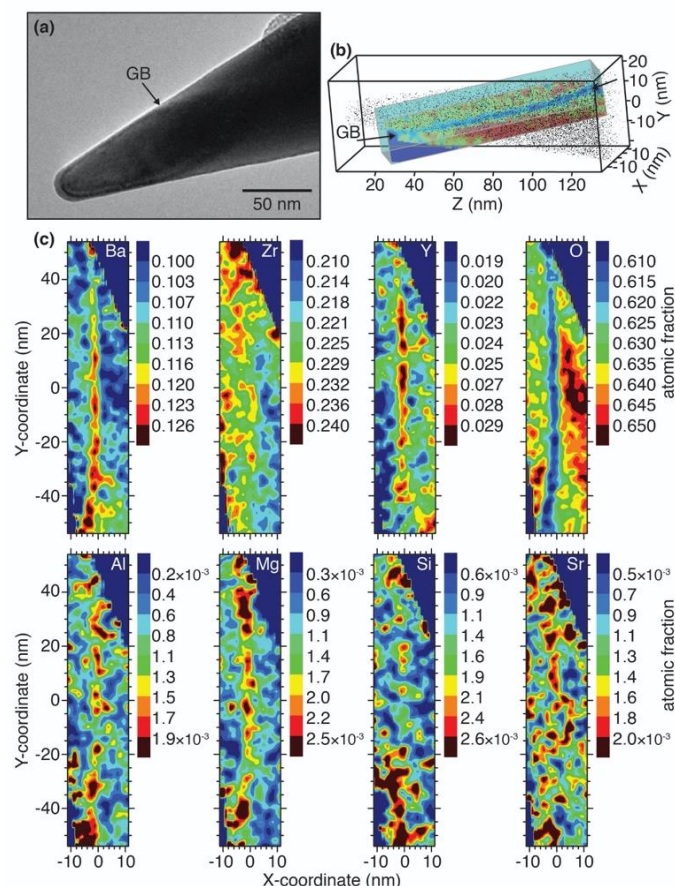


Fig. 4. APT analysis of HT1. (a) Transmission electron microscopy (TEM) micrograph pre-APT analysis. (b) Region of interest (ROI) used for (c) elemental atomic fraction 2-D contour maps of Ba, Zr, Y, O, Al, Mg, Si and Sr.

Impurity GB segregation behavior was also not consistent between specimens. The main impurities found in the HT specimens were Al, Mg, Si, and Sr at concentration levels varying from approximately 200-5500 ppm. The Si impurity was present at the greatest concentrations, ~ 600 - 5500 ppm. Both the HT1 and HT2 specimens showed Mg accumulation at the GB (200-300 ppm in the bulk vs. 1400-2000 ppm at the GB), while the HT2 sample also showed Si accumulation (~ 2200 ppm bulk vs. ~ 5500 ppm GB). Mg is a known impurity in many of the BZY elemental precursors, including BaCO_3 . A small degree of Al GB accumulation was measured in all three HT specimens, although it is only visually apparent in the elemental contour map of the HT1 sample (Fig. 4c, ~ 200 - 600 ppm bulk vs. ~ 1400 - 1900 ppm GB). As with the SPS sample, we hypothesize that the Al impurity is likely imparted by calcination in an alumina crucible and the small amount of Al impurity found in ZrO_2 precursors. Sr, the main impurity found in the BaCO_3 precursor (see Supplementary Information), was also found in every HT

ARTICLE

Journal of Materials Chemistry C

specimen (500-5500 ppm), although Sr GB segregation was not observed.

3.4 APT of the SSR-Ni sample

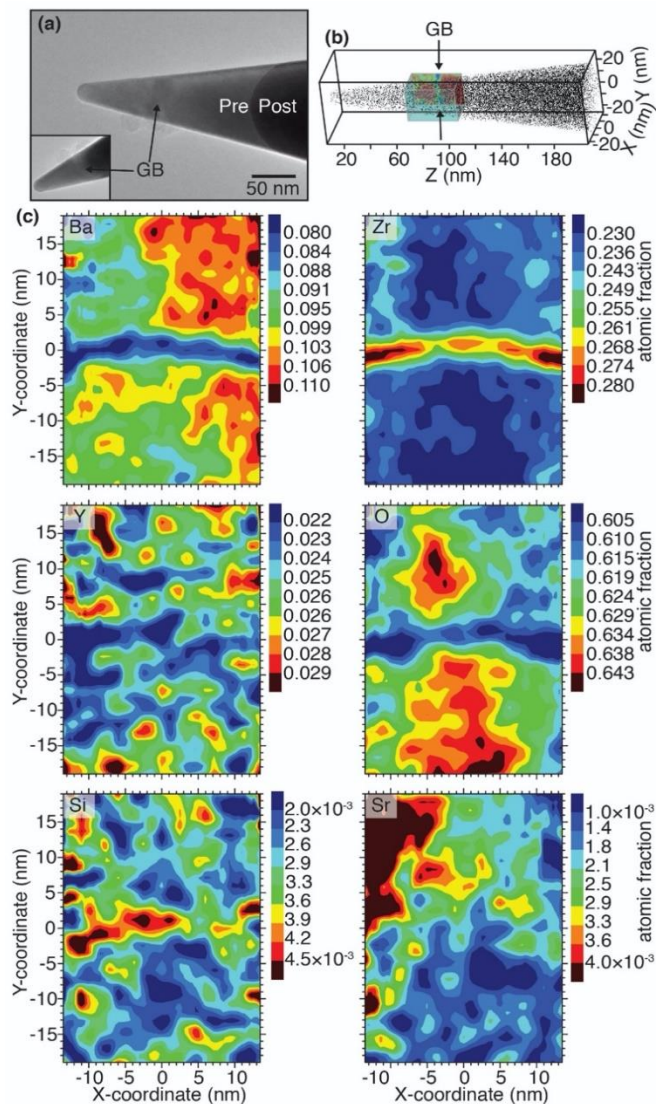


Fig. 5. APT analysis of HT3. (a) Transmission electron microscopy (TEM) micrograph pre-APT analysis. (b) Region of interest (ROI) used for (c) elemental atomic fraction 2-D contour maps of Ba, Zr, Y, O, Al, Mg, Si and Sr.

Two different GBs from the SSR-Ni sample were examined by APT; these two specimens (SSR-Ni1 and SSR-Ni2) showed similar GB chemistry (Fig. 6 and Fig. S8, respectively). Both specimens showed Zr and O depletion at the GB coupled with Ba and Y accumulation. The main impurities found in the SSR-Ni specimens were Ni (intentionally added as a sintering aid at 1 wt. %) and Si. The Ni concentration varied from approximately 0.4 at. % (in the bulk) to as much as 4.5 at. % (at the GB), while the Si concentration varied from approximately 2000 to 8000 ppm. Ni accumulation was observed as a consistent and relatively uniform layer along both GBs (e.g., Fig. 7 showing Ni accumulation at the GB of the SSR-Ni1 sample), while Si accumulation at the GB was found only for the SSR-Ni1 sample (~2000-4000 ppm in the bulk vs. 6000-7000 ppm at the GB).

3.5 APT of the SSRS-Ni sample

Only one specimen was successfully measured by APT from the SSRS-Ni sample. With the combination of a lower grain boundary density (higher average grain size) and Ni-rich grain-

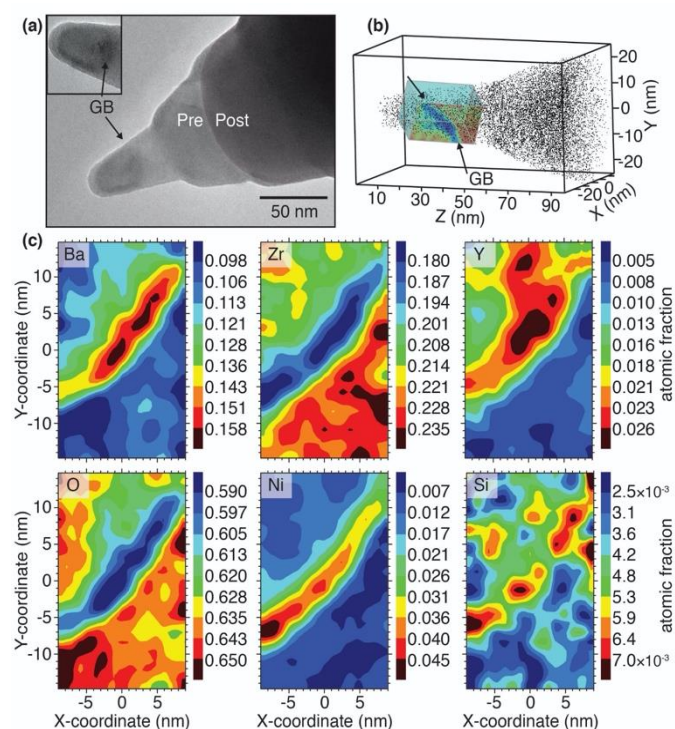


Fig. 6. APT analysis of SSR-Ni1. (a) Transmission electron microscopy (TEM) micrographs pre- and post-APT analysis (inset shows more detailed view of GB). (b) Region of interest (ROI) used for (c) elemental atomic fraction 2-D contour maps of Ba, Zr, Y, O, Ni, and Si.

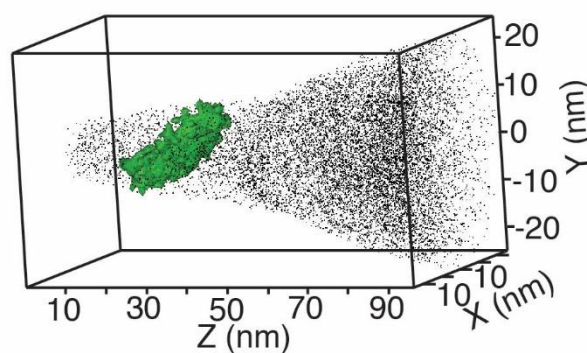


Fig. 7. Example of GB ROI selection for SSR-Ni1 using a Ni isoconcentration (> 0.6 at. %) surface. Mass spectra were analyzed and decomposed inside and outside of the region of interest.

boundary particles leading to mechanically weakened grain boundaries, the probability of successful APT experiments for the SSRS-Ni sample was lower and therefore unfortunately yielded only one successful experiment. This specimen showed Ba, Zr, and O depletion in concert with Y accumulation at the GB (Fig. 8). In addition to the major constituents, many impurities were found within this specimen, including Al, Fe, Si, and Sr (at concentrations ranging from 1500-16000 ppm) and Ni (intentionally added as a sintering aid at 1 wt. %). All of these impurities showed segregation at the GB, with the Fe and Ni manifesting as particle-shaped impurities at the GB, as shown

in Fig. 9. The Ni-rich particles were 5-10 nm in size. Since Fe is the most common impurity in NiO, it is unsurprising that these Ni-rich GB particles also contain Fe. Previously, Ricote et al. showed these Ni particles to be uniformly distributed at the GB

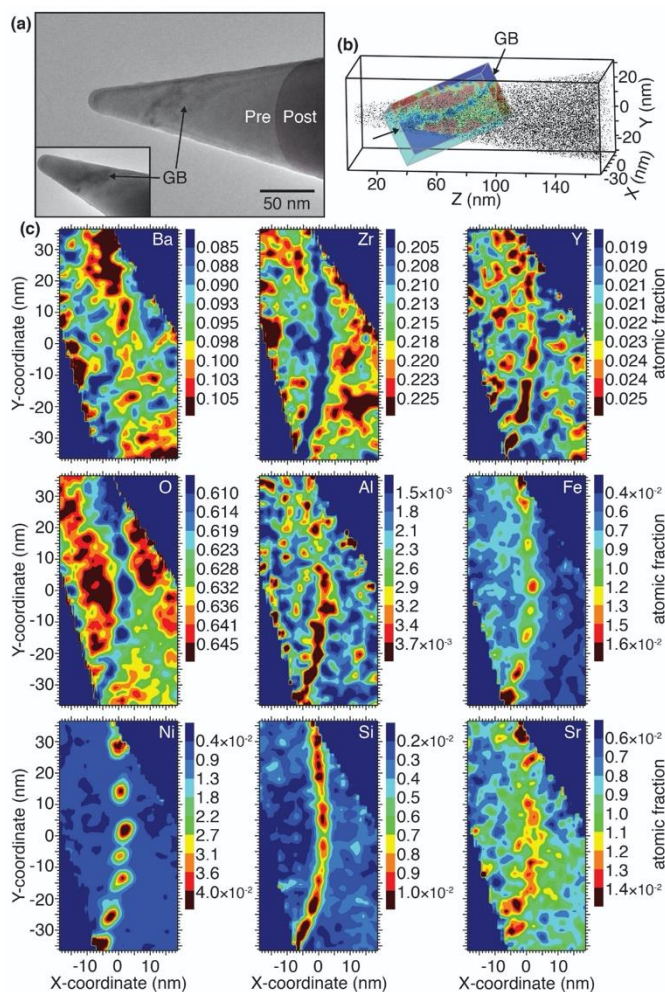


Fig. 8. APT analysis of SSRS-Ni. (a) Transmission electron microscopy (TEM) micrographs pre- and post-APT analysis (inset shows more detailed view of GB). (b) Region of interest (ROI) used for (c) elemental atomic fraction 2-D contour maps of Ba, Zr, Y, O, Al, Fe, Ni, Si, and Sr.

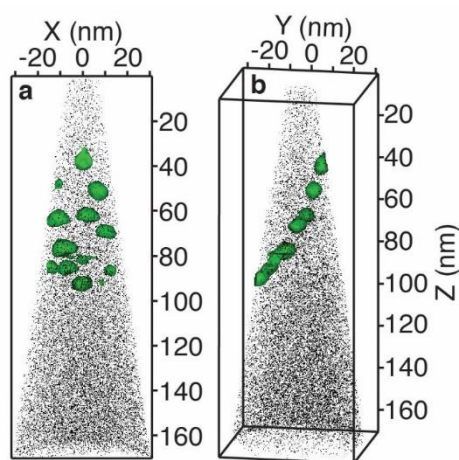


Fig. 9. Ni-rich particles in SSRS-Ni. (a) and (b) two orthogonal views of the reconstruction of the Ni-rich particles at the SSRS grain boundary. Green particles are Ni-rich regions defined by a 1 at. % isoconcentration surface.

via SEM, and these were interpreted as metallic Ni nanoparticles.¹⁸ While it is possible that Ni metal nanoparticles may be present at other GBs, the APT analysis of the GBs investigated here suggests that these particles are more likely to be NiO, as suggested in Fig S9. This is despite the fact that these samples were analyzed after long-duration conductivity testing in reducing (5% H₂) environments. Similar NiO particles have been previously reported at the GB of BCZY27 with Ni (incorporated from the anode substrate during sintering) after exposure to long duration (over 300 hours) reducing environments.²⁵ See Supplementary Information for more detail on the Ni-rich particle analysis.

3.5 Discussion of the grain-boundary chemistry results

Fig. 10a presents the ratio of GB to bulk concentration ($[GB]/[Bulk]$) for the four constituent elements (Ba, Zr, Y, and O) as well as the most common impurity elements (Al, Fe, Mg, Ni, Si, and Sr) observed across all investigated specimens. Fig. 10b presents the absolute GB concentration values measured for all specimens in a similar manner. For this data in tabular form, see Table S5 and Table S6. Based on these summary figures, a number of general observations can be drawn:

- BZY10 grain-boundary chemistry is surprisingly variable, even within the same sample. For example, even though the three grain boundaries examined in the HT sample were located only a few microns apart from one another, they showed dramatically different GB chemistry. HT1 and HT2 showed Zr and O depletion coupled with Ba and Y accumulation, while HT3 showed Ba, Y, and O depletion and Zr accumulation. One possibility is that GB orientation may play an important role in determining GB chemistry, as has been observed for other oxides^{32,33}.
- Regardless of the segregation behavior of the other primary constituent atoms in BZY10, oxygen GB depletion was observed for every specimen. This finding is consistent with the widely-accepted positive space-charge-layer description of BZY grain boundaries.^{34–41} Other than the SSRS-Ni sample, which had the largest oxygen GB depletion and the correspondingly highest GB resistance, a broader correlation could not be drawn to connect the oxygen stoichiometry at the GB with the resulting macroscopic electrical properties.
- While there is little apparent trend between the electrical properties and the oxygen GB stoichiometry, we observe a trend between the absolute concentration of Ba at the GB and the resulting electrical properties of the sample. Specifically, the average Ba GB concentrations measured for SSRS-Ni, HT, SPS, and SSRS-Ni samples were 9.0, 10.8, 11.4, and 14.5 at. % while the corresponding GB barrier heights (ϕ) calculated by Ricote et al.¹⁸ for these samples were 40, 150, 170, and 200 mV, respectively (see Table S4). This trend also applied to the measured GB activation energy for these samples ($E_{a,spGB}$). Interestingly, Ba depletion at GBs has previously been proposed as a possible cause of high GB resistance,¹⁷ but in this study, we observed the opposite trend. Of the four constituent lattice elements in BZY (Ba, Zr, Y, and O), Ba showed the most severe

GB segregation behavior, although the direction of Ba segregation varied from GB to GB.

• All of the specimens except for one (HT3) showed Zr depletion and Y accumulation at the GB. The most severe Zr depletion and Y accumulation occurred in SSR-Ni sample, which also demonstrated the highest GB-to-bulk resistance ratio (R_{GB}/R_{bulk}). This sample also showed the largest oxygen depletion (or $V_{\dot{O}}$ accumulation) at the GB, which is consistent with oxygen vacancy charge compensation of the B-site Y dopants (i.e., $Y_2O_3 \xrightarrow{2BaZrO_3} 2Y_{Zr} + V_{\dot{O}} + 3O_{\dot{O}}$). The correlation between Y GB accumulation and Zr depletion (or vice-versa for sample HT3) is consistent with the fact that they compete for the same lattice site (the B-site).

materials, at concentrations of up to 4.5 atomic percent. Segregation is more severe for SSRS-Ni (and results in Ni-rich GB nanoparticles) while the SSR-Ni sample manifests a Ni-rich film at GBs. Ni-rich GB films have been reported for SSR-Ni fabricated $BaCe_{0.7}Zr_{0.1}Y_{0.1}Yb_{0.1}O_{3-6}$ proton-conducting ceramics,⁴² while Ni-rich GB nanoparticles have been observed in SSRS-Ni fabricated $BaCe_{0.7}Zr_{0.2}Y_{0.1}O_{3-6}$.²⁵ As the SSRS-Ni sample yielded the lowest R_{GB}/R_{bulk} ratio while the SSR-Ni sample yielded the highest R_{GB}/R_{bulk} ratio, it is possible that Ni-rich GB nanoparticles are beneficial to conductivity while a continuous Ni-rich GB film is detrimental. As has been previously hypothesized, the Ni-rich GB phase may induce its own space-charge region due to differences in material work

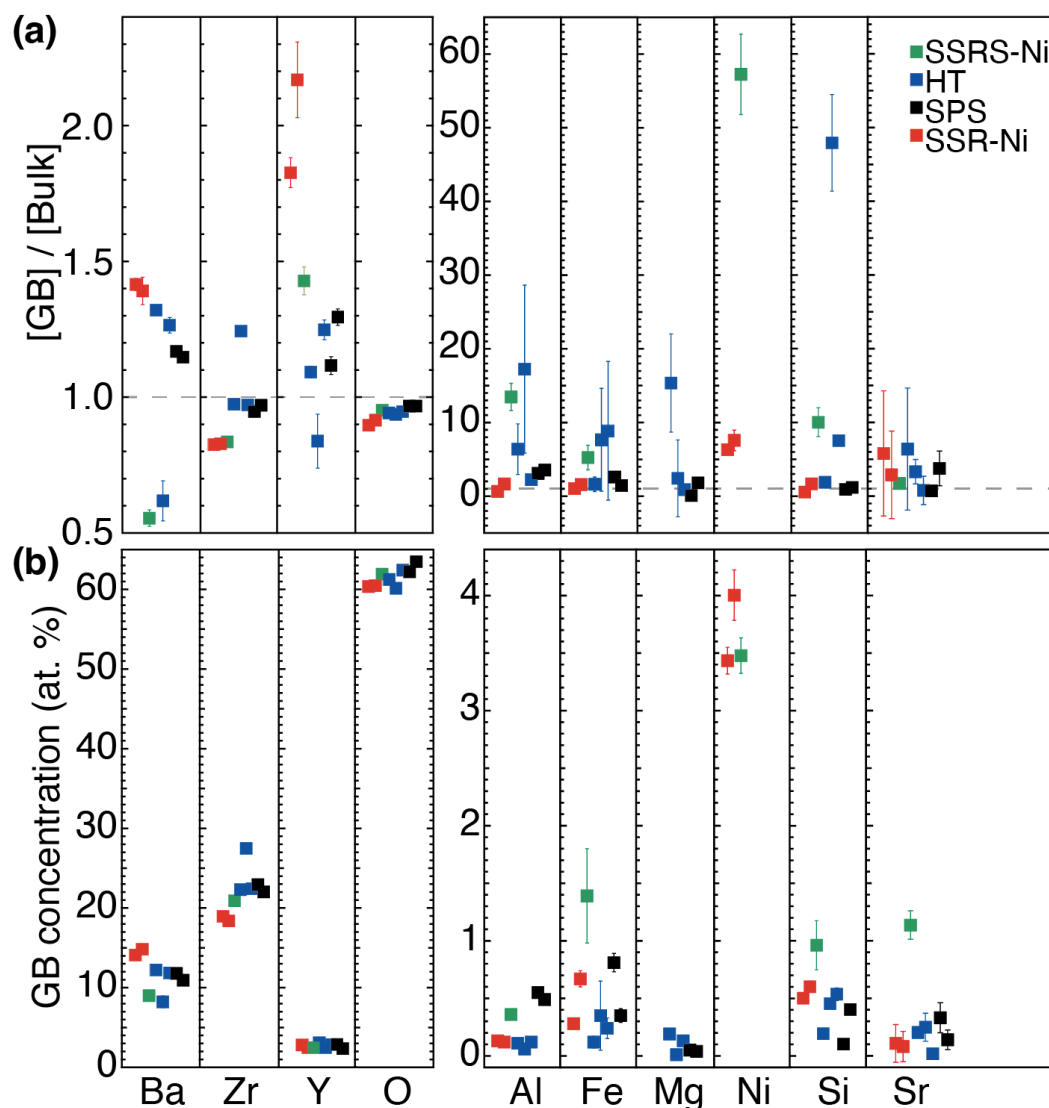


Fig. 10. (a) Ratio of grain boundary to bulk concentration. A ratio greater than 1 indicates segregation to the GB, a ratio less than 1 indicates depletion from the GB. (b) Absolute concentration at the GB of Ba, Zr, Y, O, Al, Fe, Mg, Ni, Si, and Sr for all SPS, HT, SSRS-Ni, and SSR-Ni specimens. See Table S5 and Table S6 for tabular values. Error bars are not shown in cases where the error bars are smaller than the data points.

• The samples that used NiO as a sintering aid (SSR-Ni and SSRS-Ni) tended to show the largest GB segregation effects for the constituent lattice elements, suggesting that the NiO sintering aid enhances cation-lattice mobility. Ni also preferentially segregates to the GB in the NiO-sintered

functions⁴³. While Ni-rich nanoparticles may provide a percolating space-charge pathway across the GB that assists proton transport, a homogenous Ni-rich GB film may impede proton transport. The difference in the formation of nickel nanoparticles versus a nickel-rich film may be due to the lack of

formation of BaY_2NiO_5 , which is the liquid phase reported as responsible for sintering and phase formation in SSRS, while not found in SSR, since the perovskite phase is already formed.⁴⁴

In general, impurity species were observed to accumulate at (rather than deplete from) GBs. Due to the higher energy at the GB, this is expected and has been previously observed.^{45,46} Commonly detected impurities included Al, Si, Mg, Fe, and Sr. Impurity species were generally present (0.01–1.6 atomic percent). The precursor powders are the likely source of the Mg and Sr impurities, while Al is ascribed to the use of alumina sintering containers/setters and impurities from the ZrO_2 precursors. Si is ascribed to contamination from the quartz-based mortar and pestle used during synthesis and/or volatilization from MoSi_2 furnace heating elements. Only the samples sintered with NiO showed Fe impurities. Fe is the most common impurity in NiO (see Supplementary Information for details), and thus, this is the likely source of this impurity. The HT process leads to the most marked impurity GB segregation effects, which we ascribe to the enhanced cation mobility provided by the high-temperature annealing step used for this sample. Sr segregation and Ba segregation were correlated—specimens that showed the most Ba segregation also showed the most Sr segregation. This correlation is reasonable given that Sr is the most common impurity found in the Ba precursors (it is present in concentrations up to 0.7 at. %), and it substitutes for Ba on the A-site of the perovskite lattice.

Conclusions

A richer understanding of GB chemistry is vital to further improve the performance of proton-conducting perovskites. This study demonstrates the complex nature of GB chemistry associated with these multi-cation oxide materials and suggests that Ba enrichment/depletion at the GB may be at least partially correlated to the resulting electrical properties. In addition, a surprising number of impurities, including Al, Si, Mg, and Sr were demonstrated to segregate to the GBs of these BZY10 samples, although their impact (if any) on the electrical properties of the material is unclear. Finally, Ni, in the form of NiO particles appears to lead to much less resistive GBs, while Ni in the form of a homogeneous Ni-rich GB film appears to be associated with highly blocking GBs. While this study gives a glimpse into the complexity of GB chemistry in BZY, we caution that the limited number of specimens analyzed prevents statistically relevant quantification. The difficulty associated with successfully preparing and analyzing multiple APT specimens will likely make any attempt at statistical quantification of GB chemistry extremely challenging. However, in the future, we suggest that the combination of in-situ TEM measurements of GB orientation combined with APT analysis of GB chemistry could provide further insight into potential GB structure-chemistry correlations in these materials⁴⁷.

Conflicts of interest

There are no conflicts to declare.

Acknowledgments

Research primarily supported as part of the Hydrogen in Energy and Information Sciences (HEISs) EFRC, an Energy Frontier Research Center funded by the U.S. Department of Energy (DOE), Office of Science, Basic Energy Sciences (BES), under Award # DE-SC0023450 (data analysis, interpretation), and the Army Research Office under grant number W911NF-22-1-0273 (sample fabrication and APT measurement). The atom probe instrument used in this research was supported under NSF Award No. 1040456. Computational resources were provided by NSF-MRI Grant No. CNS-0821794, MRI-Consortium: Acquisition of a Supercomputer by the Front Range Computing Consortium (FRCC), with additional support from the University of Colorado and NSF sponsorship of the National Center for Atmospheric Research, and the Colorado School of Mines Foundation, Protonic Capital Funds. The authors thank Anthony Manerbino and Coorstek for helping with the XRF analysis.

References

- 1 H. Iwahara, T. Esaka, H. Uchida and N. Maeda, *Solid State Ionics*, 1981, **3–4**, 359–363.
- 2 K. D. Kreuer, *Annu. Rev. Mater. Res.*, 2003, **33**, 333–359.
- 3 I. Zvonareva, X. Z. Fu, D. Medvedev and Z. Shao, *Energy Environ. Sci.*, 2022, **15**, 439–465.
- 4 H. Ding, W. Wu, C. Jiang, Y. Ding, W. Bian, B. Hu, P. Singh, C. J. Orme, L. Wang, Y. Zhang and D. Ding, *Nat. Commun.*, , DOI:10.1038/s41467-020-15677-z.
- 5 E. Fabbri, D. Pergolesi and E. Traversa, *Chem. Soc. Rev.*, 2010, **39**, 4355.
- 6 H. Malerød-Fjeld, D. Clark, I. Yuste-Tirados, R. Zanón, D. Catalán-Martínez, D. Beeaff, S. H. Morejudo, P. K. Vestre, T. Norby, R. Haugsrud, J. M. Serra and C. Kjølseth, *Nat. Energy*, 2017, **2**, 923–931.
- 7 C. Duan, J. Tong, M. Shang, M. Sanders, S. Ricote and R. O'Hayre, *Science (80-.)*.
- 8 C. Duan, R. J. Kee, H. Zhu, C. Karakaya, Y. Chen, S. Ricote, A. Jarry, E. J. Crumlin, D. Hook, R. Braun, N. P. Sullivan and R. O'Hayre, *Nature*, 2018, **557**, 217–222.
- 9 S. Choi, C. J. Kucharczyk, Y. Liang, X. Zhang, I. Takeuchi, H. Il Ji and S. M. Haile, *Nat. Energy*, 2018, **3**, 1–9.
- 10 E. Vøllestad, R. Strandbakke, M. Tarach, D. Catalán-Martínez, M. L. Fontaine, D. Beeaff, D. R. Clark, J. M. Serra and T. Norby, *Nat. Mater.*, 2019, **18**, 752–759.
- 11 D. Medvedev, *Int. J. Hydrogen Energy*, 2019, **44**, 26711–26740.
- 12 D. Clark, H. Malerød-Fjeld, M. Budd, I. Yuste-Tirados, D. Beeaff, S. Aamodt, K. Nguyen, L. Ansaloni, T. Peters, P. K. Vestre, D. K. Pappas, M. I. Valls, S. Remiro-Buenamañana, T. Norby, T. S. Bjørheim, J. M. Serra and C. Kjølseth, *Science (80-.)*, 2022, **376**, 390–393.
- 13 H. Iwahara, H. Uchida, K. Ono and K. Ogaki, *J. Electrochem. Soc.*, 1988, **135**, 529.
- 14 M. J. Scholten, J. Schoonman, J. C. van Miltenburg and E. H. P. Cordfunke, *Thermochim. Acta*, 1995, **268**, 161–168.
- 15 C. W. Tanner and A. V. Virkar, *J. Electrochem. Soc.*, 1996,

- 143**, 1386–1389.
- 16 K. Katahira, Y. Kohchi, T. Shimura and H. Iwahara, *Solid State Ionics*, 2000, **138**, 91–98.
- 17 P. Babilo, T. Uda and S. M. Haile, *J. Mater. Res.*, 2007, **22**, 1322–1330.
- 18 S. Ricote, N. Bonanos, A. Manerbino, N. P. Sullivan and W. G. Coors, *J. Mater. Chem. A*, DOI:10.1039/c4ta02848a.
- 19 S. Ricote, N. Bonanos, H. J. Wang and B. A. Boukamp, *Solid State Ionics*, 2012, **213**, 36–41.
- 20 S. B. C. Duval, P. Holtappels, U. F. Vogt, E. Pomjakushina, K. Conder, U. Stimming and T. Graule, *Solid State Ionics*, 2007, **178**, 1437–1441.
- 21 J. H. Tong, D. Clark, M. Hoban and R. O’Hayre, *Solid State Ionics*, 2010, **181**, 496–503.
- 22 E. W. Müller, *Rev. Sci. Instrum.*, 1968, **39**, 83.
- 23 T. F. Kelly and M. K. Miller, *Rev. Sci. Instrum.*, 2007, **78**, 031101.
- 24 M. K. Miller and R. G. Forbes, *Mater. Charact.*, 2009, **60**, 461–469.
- 25 D. R. Diercks, B. P. Gorman, A. Manerbino and G. Coors, *J. Am. Ceram. Soc.*, 2014, **97**, 3301–3306.
- 26 R. Kirchhofer, M. C. Teague and B. P. Gorman, *J. Nucl. Mater.*, 2013, **436**, 23–28.
- 27 R. Kirchhofer, D. R. Diercks, B. P. Gorman, J. F. Ihlefeld, P. G. Kotula, C. T. Shelton and G. L. Brennecke, *J. Am. Ceram. Soc.*, 2014, **97**, 2677–2697.
- 28 R. Agrawal, R. A. Bernal, D. Isheim and H. D. Espinosa, *J. Phys. Chem. C*, 2011, **115**, 17688–17694.
- 29 A. Devaraj, R. Colby, W. P. Hess, D. E. Perea and S. Thevuthasan, *J. Phys. Chem. Lett.*, 2013, **4**, 993–998.
- 30 D. R. Diercks, B. P. Gorman, R. Kirchhofer, N. Sanford, K. Bertness and M. Brubaker, *J. Appl. Phys.*, 2013, **114**, 184903.
- 31 L. Mancini, N. Amirifar, D. Shinde, I. Blum, M. Gilbert, A. Vella, W. Lefebvre, R. Larde, E. Talbot, P. Pareige, X. Portier, A. Ziani, C. Davesne, C. Durand, J. Eymery, N. Grandjean and L. Rigutti, *J. Phys. Chem. C*, 2014, **118**, 24136–24151.
- 32 Y. Pang, and P. Wynblatt, *J. Am. Cer. Soc.*, 2005, **88**, 2286–2291.
- 33 N. Shibata et al., *Phil. Mag.*, (2004), **84**, 2381–2415.
- 34 F. Iguchi, N. Sata and H. Yugami, *J. Mater. Chem.*, 2010, **20**, 6265–6270.
- 35 C. Kjølsseth, H. Fjeld, Ø. Prytz, P. I. Dahl, C. Estournès, R. Haugsrud and T. Norby, *Solid State Ionics*, 2010, **181**, 268–275.
- 36 C.-T. Chen, C. E. Danel and S. Kim, *J. Mater. Chem.*, 2011, **21**, 5435.
- 37 F. Iguchi, C.-T. Chen, H. Yugami and S. Kim, *J. Mater. Chem.*, 2011, **21**, 16517.
- 38 M. Shirpour, R. Merkle, C. T. Lin and J. Maier, *Phys. Chem. Chem. Phys.*, 2012, **14**, 730–40.
- 39 M. Shirpour, R. Merkle and J. Maier, *Solid State Ionics*, 2012, **216**, 1–5.
- 40 A. Lindman, E. E. Helgee and G. Wahnström, *Solid State Ionics*, 2013, **252**, 121–125.
- 41 E. E. Helgee, A. Lindman and G. Wahnström, *Fuel Cells*, 2013, **13**, 19–28.
- 42 D. Clark, J. Tong, A. Morrissey, A. Almansoori, I. Reimanis and R. O’Hayre, *Phys. Chem. Chem. Phys.*, 2014, **16**, 5076–80.
- 43 A. V Chadwick and S. L. P. Savin, *Solid State Ionics*, 2006, **177**, 3001–3008.
- 44 J. H. Tong, D. Clark, L. Bernau, M. Sanders and R. O’Hayre, *J. Mater. Chem.*, 2010, **20**, 6333–6341.
- 45 M. Aoki, Y.-M. Chiang, I. Kosacki, L. J.-R. Lee, H. Tuller and Y. Liu, *J. Am. Ceram. Soc.*, 1996, **79**, 1169–1180.
- 46 S. B. C. Duval, P. Holtappels, U. Stimming and T. Graule, *Solid State Ionics*, 2008, **179**, 1112–1115.
- 47 G. L. Burton, S. Ricote, B. J. Foran, D. R. Diercks and B. P. Gorman, *J. Am. Ceram. Soc.*, DOI:10.1111/jace.17014.